Construction and Building Materials 495 (2025) 143596

Contents lists available at ScienceDirect

Construction and Building Materials

journal homepage: www.elsevier.com/locate/conbuildmat

# Blending additional calcium hydroxide into LC$^3$ with high amount of calcined clay to modify fresh and hardened properties

Yu Chen [a,*], Yu Zeng [b,*], Minfei Liang [c], Shan He [b], Oğuzhan Çopuroğlu [b]

[a] State Key Laboratory of Engineering Materials for Major Infrastructure, School of Material Science and Engineering, Southeast University, Nanjing, China
[b] Microlab, Faculty of Civil Engineering and Geosciences, Delft University of Technology, Delft, the Netherlands
[c] Clarendon Laboratory, Department of Physics, University of Oxford, Oxford, UK

ARTICLE INFO

*Keywords:*
Hydrated lime
LC3
Rheology
Hydration
Pore structure

ABSTRACT

Adding hydrated lime (CH) into blended cement incorporating high volume of Supplementary Cementitious Materials (SCMs) is a viable method to provide the necessary calcium hydroxide for the pozzolanic reaction, thereby improving the mechanical performance at later stages. However, the effects of relatively small dosages of CH on the rheological properties and resulting microstructure of limestone-calcined clay cement (LC3) remain unclear. This paper aims to investigate the influence of a small CH addition on the fresh and hardened properties of LC3 systems, in which Portland cement is largely replaced (80 wt%) by limestone and calcined clay. The results indicate that the additional CH notably reduces the water film thickness, leading to increased dynamic yield stress, plastic viscosity and re-flocculation. A delay in the elasticity development and static yield stress evolution within the first 1.5 h was observed with the addition of 2.5 wt% CH, attributed to the initial dissolution of CH, which is mitigated by using 10 wt% CH. Furthermore, additional CH accelerated early-age hydration and facilitated long-term pozzolanic reactions, resulting in the increased amount of C-(A)-S-H gel and AFm phases, and reduced porosities after 7 and 28 days. These chemical effects could well compensate the high air void content caused by the high viscosity, and therefore contributes to mortars with higher compressive strengths than plain LC3 at later ages.

## 1. Introduction

To reduce $CO_2$ emissions of cement industry, rapidly growing attention has been paid to develop and use blended cementitious materials containing a relatively high volume of supplementary cementitious materials (SCMs) and Portland cement or clinker [1–3]. However, common SCMs, i.e., blast-furnace slag, fly ash and silica fume, are limited available for the use of blended cement for a long term [4,5]. Due to the abundant deposit, limestone and calcined clay have been considered as the most promising sustainable binding materials [5–7]. Metakaolin, the main reactive phase in calcined kaolinitic clay, is rich in reactive aluminate and silicate, and therefore able to react with calcium hydroxide (CH) from the hydration of clinker to generate C-A-S-H gel and strätlingite. AFm phases, i.e., hemi/mono-carboaluminate, are also formed if the calcite is presented in the system [8,9]. The above-mentioned pozzolanic reactions are beneficial to refine the capillary pores for improving hardened properties (e.g., mechanical performance and durability) of cementitious materials [10,11].

Limestone-calcined clay cement (LC3) refers to a ternary cement blend incorporating calcined clay, and limestone [12]. A typical formulation, LC3–50, consists of 15 wt% limestone, 30 wt% calcined clay, 5 wt% gypsum, and 50 wt% clinker, which has been applied in the industry trial in many countries, such as India [13,14], Cuba [15], Colombia, France and Ivory Coast [16]. LC3–50 appears to be less sustainable compared to CEM III/B–C cements (slag cement) that has less than 35 wt% of clinker while independency to gradually decreasing availability of blast furnace slag is considered advantageous [17]. However, as reported by earlier studies [18,19], substituting more than 50 wt% of clinker with limestone and calcined clay can negatively affect clinker hydration and pozzolanic reaction, resulting in a significant decrease in mechanical performance. Adding hydrated lime in the mixture incorporating high content of SCMs is a viable strategy to provide sufficient calcium hydroxide required for the pozzolanic reaction for enhancing the strength of hardened material. This approach has been

* Corresponding authors.
*E-mail addresses:* y_chen@seu.edu.cn (Y. Chen), Y.Zeng-4@tudelft.nl (Y. Zeng), minfei.liang@physics.ox.ac.uk (M. Liang), S.He-2@tudelft.nl (S. He), O.Copuroglu@tudelft.nl (O. Çopuroğlu).

https://doi.org/10.1016/j.conbuildmat.2025.143596
Received 16 April 2025; Received in revised form 1 July 2025; Accepted 10 September 2025
Available online 15 September 2025

implemented in formulating a quaternary blend of ultrahigh-performance concrete (fly ash, slag, silica fume and Portland cement) [20]. The authors [20] pointed out that the use of hydrated lime largely facilitates the pozzolanic reaction, contributing to archiving a denser microstructure and better mechanical properties. Jaafri et al. [21] reported the impacts of adding a high content of hydrated lime (12.5–50 wt% of the binder) on the fresh and hardened behaviors of plain Portland cement mortars and limestone-blended mortars. In their case, SCMs were not included in the binding material. Hu et al. [22] found that by using external gypsum and portlandite, LC3 mixture with 75 wt% of clinker substitution can reach more than 40 MPa after 28 days.

It should be noted that the $CO_2$ emissions from producing hydrated lime are higher than those from producing clinker [23]. The incorporation of hydrated lime in LC3 may therefore increase the global warming potential (GWP). However, improvements in mechanical properties at later ages, resulting from enhanced pozzolanic reactions facilitated by the addition of hydrated lime, may partially offset the GWP increase. Sun et al. [12] reported that the GWP of LC3 incorporating portlandite is generally lower than that of Portland cement but higher than that of LC3 without portlandite. An exception was observed in a blend composed of 19.4 wt% Portland cement, 40 wt% calcined clay, 20 wt% limestone, 20 wt% portlandite, and 0.6 wt% gypsum, which showed a lower GWP than the corresponding blend without portlandite. In their study, a relatively high dosage (15–20 wt%) of portlandite was used.

On the other hand, if hydrated lime is sourced from portlandite-rich industrial waste, the $CO_2$ emissions of LC3 containing hydrated lime can be significantly reduced. Hu et al. [22] compared the $CO_2$ emissions of LC3–50 with those of LC3 incorporating 13.6 wt% hydrated lime using life cycle assessment (LCA). They found that when the hydrated lime was derived from industrial waste, the LC3 with 13.6 wt% hydrated lime achieved a 41 % reduction in $CO_2$ emissions compared to LC3–50. Overall, to ensure a low GWP for LC3 containing hydrated lime, two guidelines should be followed: (1) use a low dosage of hydrated lime (<15 wt%); and (2) source the hydrated lime preferably from portlandite-rich industrial waste. However, research to date has not yet determined the influences of adding relatively small dosages of hydrated lime/Portlandite in LC3 mixtures on rheological properties of fresh mixtures, and the resulting microstructure. As reported by Chabannes et al. [24], hydrated lime shows a relatively high specific surface area, which may significantly affect the workability of fresh LC3 with lime.

This study is set out to explore the effect of additional hydrated lime on fresh and hardened properties of LC3 materials with high amount of calcined clay. Fresh properties, including flowability and structural build-up behaviors, were assessed through rheological tests. Meanwhile, isothermal calorimetry, thermogravimetric analysis (TGA) and qualitative X-ray diffraction (XRD) were conducted to gain more insights into early-age hydration kinetics and phase assemblages. Finally, pore structures of paste and mortar specimens were characterized with

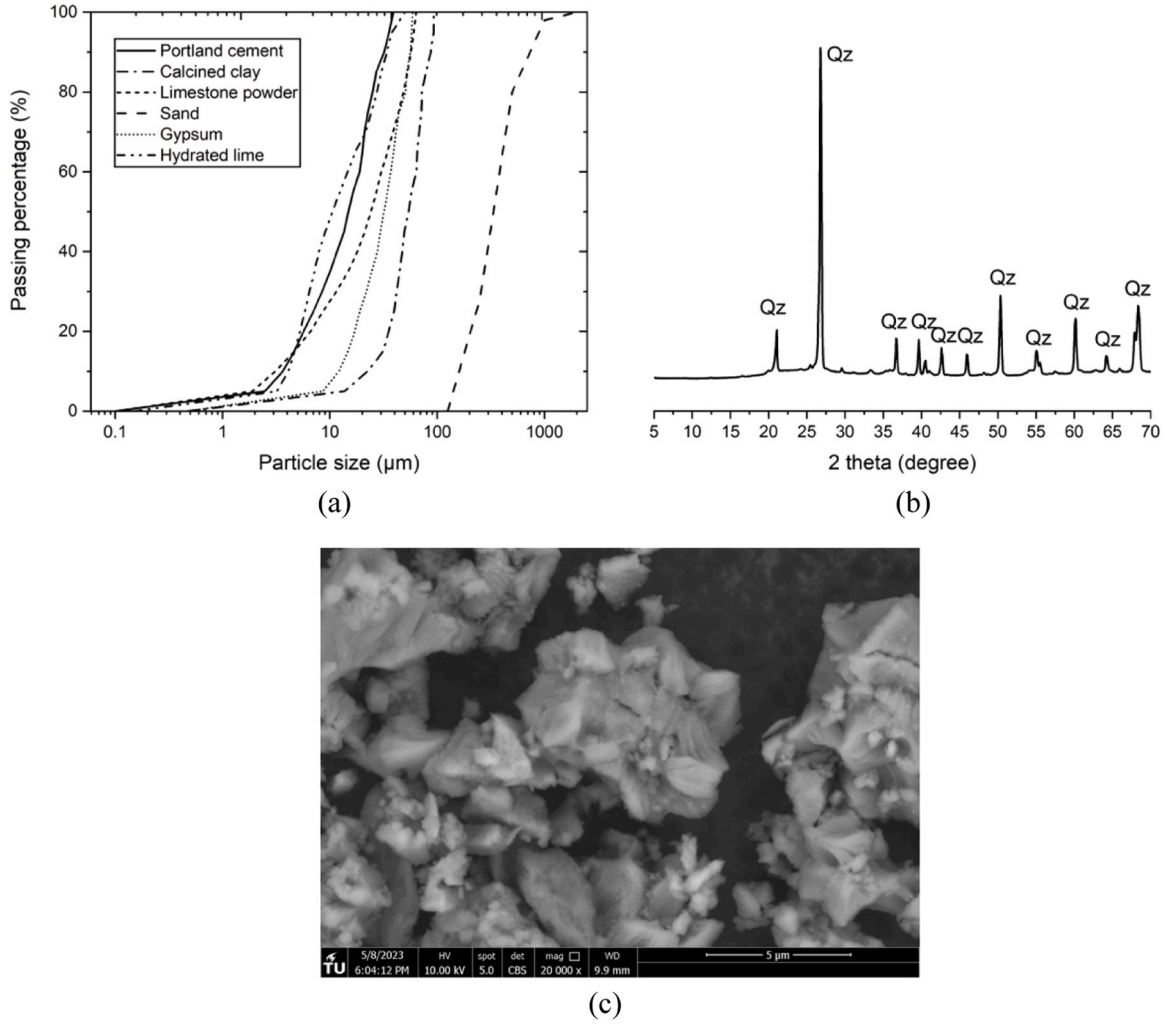


**Fig. 1.** (a) Particle size distributions of raw materials (measured through laser diffractometry). (b) X-ray diffraction pattern of calcined clay. Qz-quartz. (c) Electron micrograph of hydrated lime under secondary electron imaging mode.

mercury intrusion porosimetry (MIP) and X-ray computed tomography (X-CT) scanning, and the influence on macro compressive strength was also discussed.

## 2. Materials and methods

### 2.1. Raw materials and mix designs

Binding materials used in this research include CEM I 52.5 R Portland cement (PC), limestone powder (LS), calcined clay (CC), gypsum and CL-90S hydrated lime (CH). Gypsum with more than 99 % purity is purchased from Merck KGaA, Germany. CC, which is mainly consisted of metakaolin and quartz, is provided by Argeco, France. CH is produced by Lhoist, Belgium. Particle size distributions of all fines were measured through laser diffractometry and presented in Fig. 1(a). Compared to other fines, CC contains more coarse particles, but this does not necessarily mean the specific surface area (SSA) of CC should be smaller. Instead, due to the existence of fine metakaolin particles, SSA of CC is one order larger than those of PC, LS and gypsum (Table 1). Furthermore, even though particle sizes of CH and PC are similar, the former has a significantly larger SSA, and this phenomenon is mainly attributed to the porous morphology of CH particles (Fig. 1(c)).

Oxide compositions of CC, LS, PC and CH are presented in Table 2. Among them, LS, PC and CH are mainly composed of crystalline phases, while CC contains 34.2 wt% of crystalline quartz and 64.1 wt% of amorphous phases (determined through Rietveld refinement of the XRD pattern, shown in Fig. 1(b)). To confirm the reactivity of the calcined clay, a chemical dissolution test was conducted following NEN-EN 196–2 [25]. The reactive content of calcined clay was about 48.8 wt%.

As shown in Table 3, all mixtures contain 20 wt% of PC and 50 wt% of CC. To avoid sulfate depletion occurring before or during the main hydration peak, additional gypsum is considered, and it also helps to improve the early-age compressive strength of hardened binders [6,19]. The amount of additional gypsum was determined by a preliminary isothermal calorimetry screening. It should be noted that, this research was carried out to investigate the influence of CH, so a longer interval between the main hydration peak and the alumina peak was preferred to better clarify differences among mixtures. Hence, 4 wt% of additional gypsum, which could effectively postpone the aluminate peak (shown in Fig. 2) was adopted as the benchmark in this research.

The total content of LS and CH was fixed to 26 wt% of binder in all the mixtures. For C2.5 and C10, 2.5 wt% and 10 wt% CH were added respectively, and the LS content dropped to 23.5 wt% and 16 wt% correspondingly. The water-to-binder mass ratio was kept a constant (0.3), and 1 wt% polycarboxylate ether (PCE)-based superplasticizer (SP) was added.

Mortar samples with a binder-to-aggregate ratio of 1.5 were prepared for compressive strength tests and X-CT scanning, while paste samples were prepared for all the other tests. In the former, quartz sand was used as aggregate, and the grain size was between 0.125 mm - 2 mm (see more details in Fig. 1(a)). All the samples were mixed using the same procedures: (1) dry-mixing at low speed for 1 min before adding liquid (SP+water); (2) mixing at low speed for 1.5 min while adding liquid (SP+water) at the same time; (3) pausing for 1 min to scrape the inner wall and bottom of mixing bowl; (4) mixing at high speed for 1 min. Paste and mortar samples were prepared using a small mixing machine (model IKA® T 50 ULTRA-TURRAX, 500–10000 rpm of rotational speed, 250–30000 mL of sample size, 42 mm of stirrer diameter) and a Hobart mixer (A-200-N), respectively. Time zero in this study is defined as the moment when the fresh mixture is ready.

**Table 1**
Physical characteristics of calcined clay, limestone powder, Portland cement, hydrated lime, and gypsum.

| | Calcined clay | Limestone powder | Portland cement | Gypsum | Hydrated lime |
|---|---|---|---|---|---|
| Density [g/cm$^3$] | 2.51 | 2.65 | 3.12 | 2.32 | 2.30 |
| SSA [m$^2$/g] | 10.06 | 1.22 | 1.16 | 0.53 | 13.15 |
| $D_{v50}$ [μm] | 69.35 | 24.19 | 14.86 | 31.94 | 10.54 |

**Table 2**
Oxide compositions (normalized) of calcined clay, limestone powder, Portland cement and hydrated lime.

| XRF [wt%] | Calcined clay | Limestone powder | Portland cement | Hydrated lime |
|---|---|---|---|---|
| CaO | 0.54 | 55.40 | 67.87 | 74.62 |
| $SiO_2$ | 54.38 | 0.17 | 17.20 | 0.09 |
| $Al_2O_3$ | 37.90 | 0.03 | 4.56 | 0.05 |
| $Fe_2O_3$ | 2.56 | 0.04 | 2.72 | 0.05 |
| $K_2O$ | 0.17 | 0 | 0.62 | 0.02 |
| $TiO_2$ | 1.10 | 0 | 0.34 | 0 |
| $ZrO_2$ | 0.05 | 0 | 0 | 0 |
| $SO_3$ | 0 | 0 | 2.41 | 0.05 |
| Others | 1.93 | 0 | 3.06 | 0.71 |
| L.O.I. (950°C) | 1.37 | 44.36 | 1.22 | 24.41 |
| Total | 100.00 | 100.00 | 100.00 | 100.00 |

### 2.2. Test procedures

#### 2.2.1. Characterization of rheological behaviors

Both rotational shear and oscillatory shear tests were employed to characterize fresh properties of different mixtures. All the rheological tests were performed based on an Anton Paar MCR 302e rheometer, which was equipped with a cylindrical cup (68 mm of the depth and 28.92 mm of the inner diameter) and a four-blade vane (40 mm of the height and 22 mm of the diameter). The inner surface of cylindrical cup was covered with steel lamellas to minimize the wall-slippage during testing. For each measurement, about 85 g of fresh paste was added to fill in the measuring cup. The temperature of the entire measuring cup was kept identical as 20 °C by using a refrigerated circulator produced by Julabo, Germany. Prior to the rheological test, a pre-shear session (a rotational speed of 100 min$^{-1}$ and the duration of 30 s) and 30 s of resting was applied. All rheological tests were repeated at least twice to ensure the repeatability.

*2.2.1.1. Rotational shear rheometry.* Flow curve and constant shear rate (CSR) tests were conducted consecutively to quantify rheological parameters like dynamic/static yield stress and plastic viscosity. The shear profile used in flow curve tests was adopted in Ref [26]. As shown in Fig. 3(a), the rotational speed linearly increased from 0 to 80 min$^{-1}$ and decreased in a stepwise manner. In total 14 steps (i.e., 80 / 70 / 60 / 50 / 40 / 30 / 20 / 10 / 8 / 6 / 4 / 2 / 1 / 0.1 min$^{-1}$) were set, and the duration for each step was 15 s. The flow curve test was executed at the material age of 1.15 min and lasted for about 3.75 min. After 10 min of resting time, when the material age was 15 min, the CSR test was performed with rotational velocity of 0.1 min$^{-1}$ and duration of 30 s. Afterwards, the CSR test was executed every 15 min until the material age reached 90 min. For both tests, data was collected every 0.1 s.

*2.2.1.2. Oscillatory shear rheometry.* Strain sweep and small amplitude oscillatory shear (SAOS)-time sweep tests were further conducted to gain more insights into the rheological properties. The strain sweep test was conducted to determine the linear viscoelastic domain (LVED) and critical strain (defined as the boundary of LVED) of different mixtures at a material age of 1.25 min. The applied amplitude strain was from 0.001 % to 100 % and the frequency was 1 Hz. After the strain sweep test and 30 s' resting, SAOS-time sweep was applied to monitor the evolution of the storage modulus (G′) with time. It should be noted that, G′ is an independent factor of applied strain when the applied strain is lower than the critical strain. In the current study, the applied amplitude

**Table 3**
Mixture compositions of cementitious materials (wt% of the binder).

| | Portland cement | Calcined clay | Limestone powder | Hydrated lime | Additional gypsum | Water | SP | Sand |
|---|---|---|---|---|---|---|---|---|
| C0 | 20 | 50 | 26 | 0 | 4 | 30 | 1 | 150 |
| C2.5 | 20 | 50 | 23.5 | 2.5 | 4 | 30 | 1 | 150 |
| C10 | 20 | 50 | 16 | 10 | 4 | 30 | 1 | 150 |

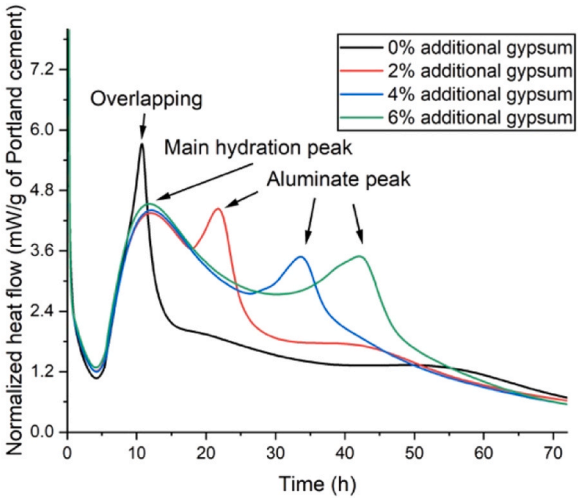


**Fig. 2.** Preliminary isothermal calorimetry screening to determine the amount of additional gypsum. Mixture compositions were provided in Table A1 (Appendix).

strain of 0.005 % (according to strain sweep test results in Section 3.1.2) and a frequency of 1 Hz were selected in the SAOS-time weep test. Such parameters were also in agreement with previous studies [19,27,28]. SAOS-time sweep test was conducted during the material age of 23–83 min and the measure value was recorded each 30 s. After that, an additional strain sweep test was conducted to assess the change in viscoelastic behaviors. Details of rheological tests were summarized in Table 4.

#### 2.2.2. Hydration kinetics and characterization of phase assemblages

The effect of CH on hydration kinetics and reaction product composition was investigated using isothermal calorimetry, TGA and XRD. The isothermal calorimetry was conducted with a TAM Air isothermal calorimeter to monitor the hydration heat evolution within the first 7 days. For each mixture, approximately 60 g fresh paste was prepared, and 6 g sample was poured into a 20 mL glass ampoule. After that, it was placed into the calorimeter together with the pre-weighted reference material (i.e., silica sand). The test was performed at 20 °C and the heat flow data was recorded every 30 s. The rest of the fresh mixture was then cured in a sealed environment.

After 60 min, 1 day, 7 days and 28 days, powder samples were obtained following the solvent exchange method recommended by RILEM TC-238 [29]. TGA of collected powder samples were conducted with Netzsch STA 449 F3 Jupiter. During the test, about 30 mg sample was heated from 40 to 1000 °C in the argon atmosphere, with a heating rate of 10 °C/min. XRD patterns were acquired using Bruker D8 advance diffractometer, with a Cu-Kα source operated at 45 kV and 40 mA. Around 1 g sample was added into the plastic sample holder and scanned from 5° to 70° 2θ, with a stepwise of 0.010° 2θ and a rate of 1 s/step. In order to quantify the amount of amorphous phases, 10 wt% silicon powder was added as the internal standard. Rietveld refinements of all the XRD profiles were conducted with Profex 5.2.

#### 2.2.3. Pore structure analysis and compressive strength test

After 7 and 28 days' hydration, small pieces with sizes of around 2 mm were collected from abovementioned paste samples. All the samples were immersed in isopropanol for three days to stop hydration and then dried in the freeze dryer for MIP tests. The contact angle between mercury and investigated materials was assumed to be 140°, and the pore size distribution between 0.007 μm and 395 μm was obtained. Both intrusion and extrusion curves were measured to assess total porosities and effective porosities.

In order to further investigate microstructures and mechanical properties at the mortar scale, prism mortar specimens (40 mm×40 mm×160 mm) were casted and cured in the moist condition (20 ± 2 °C, 99 % RH). After 28 days, cylindrical samples (25 mm in diameter and 20 mm in height) were extracted for X-ray CT scanning. The spatial resolution was 12.5 $\mu m^3$/voxel to balance the scanning efficiency and the scanning range, so voids less than 12.5 μm could not be considered in this test. In further image processing and void content assessment, the size of the region of interest (ROI) is 17 mm × 17 mm, and all the treatments were achieved with the open source ImageJ software. More details could be found in [30]. For each sample, about 1000 grayscale images were chosen to assess the air void content.

Following EN 196–1 [31], compressive strengths were measured at material ages of 1, 3, 7, 28 and 56 days to bridge early-age properties and microstructures with long-term mechanical properties. The compressive strength test was performed at a loading rate of 2.4 kN/s, and for each mixture, three replicates were measured at each age.

## 3. Results and discussions

### 3.1. Rheological behaviors

#### 3.1.1. Flow curve

Based on the predefined rotational velocities, Fig. 3(b) shows the typical torque curve measured in the flow curve test. The torque increased rapidly in the first second and then reached a peak value, suggesting the deconstruction of flocs between particles. After that, the torque decreased shortly and then increased with the rotational speed. For each rotational speed in the following stage (from 80 to 0.1 $min^{-1}$), the measured toque increased dramatically and then got relatively stabilized. Therefore, the average value of the last 50 data points (i.e., data collected in the last 5 s for each speed) was employed to represent the measured torque under the corresponding rotational speed, and test results obtained with different mixtures were summarized as Fig. 3(c) and (d). When the speed is relatively low (i.e., less than 10 $min^{-1}$), the structural rebuilding rate (i.e., re-flocculation rate) could be higher than the structural breakdown rate, so a higher torque was measured [32,33] (Fig. 3(c)). However, when the speed got higher than 10 $min^{-1}$, an opposite tendency was observed. Given that the investigated paste was in steady-state flow status, the torque increased almost linearly with the rotation speed (Fig. 3(d)). The Bingham model could be used to describe the relationship.

$$T = G + HN \tag{1}$$

where $T$ denotes the measured torque (unit: mNm), $G$ is a parameter related to yield stress (unit: mNm), $H$ represents a factor associated with plastic viscosity (unit: mNm·s), $N$ is the rotational speed (unit: $min^{-1}$). By assuming that the entire gap between the vane and measuring cell was under shear and there was no plug-flow, the relationship between the shear stress and the shear rate could be obtained with Reiner-Riwlin equations (Eqs. (2) and (3)).

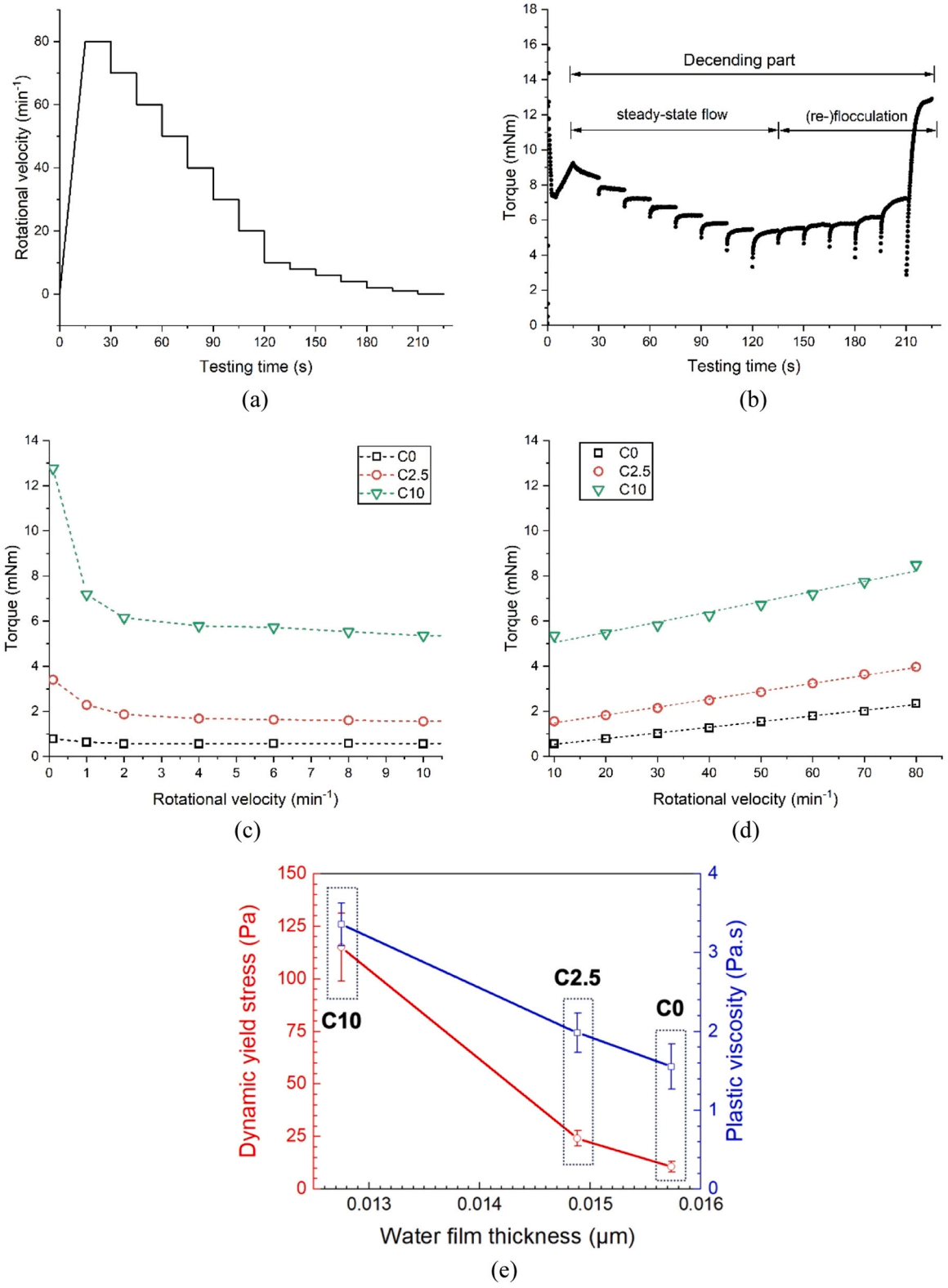


**Fig. 3.** Flow curve test: (a) Testing protocol of flow curve defined by rotational velocities; (b) A typical torque vs. testing time curve obtained using the predefined shear profile; (c) The average torque values at rotational velocities within 10 $min^{-1}$ (re-flocculation); (d) The average torque values in the range of 10–80 $min^{-1}$ rotational velocities (steady-state flow), fitted with the Bingham model; (e) The correlation between water film thickness and measured dynamic yield stress and plastic viscosity.

**Table 4**
Summary of rheological test protocols.

| Material age [min:s] | Rotational shear rheometry | Material age [min:s] | Oscillatory shear rheometry |
|---|---|---|---|
| 0:15–0:45 | Pre-shear (100 $min^{-1}$) | 0:15–0:45 | Pre-shear (100 $min^{-1}$) |
| 0:45–1:15 | Resting | 0:45–1:15 | Resting |
| 1:15–1:30 | Ramp up of shear rate from 0 to 80 $min^{-1}$ | 1:15–23:15 | Strain sweep test (0.001 %–100 %, 1 Hz) |
| 1:30–5:00 | Stepwise shear test 80/70/60/50/40/30/20/10/8/6/4/2/1/0.1 $min^{-1}$ (15 s of each step) | 23:15–23:45 | Resting |
| 5:00–15:00 | Resting | 23:45–83:45 | SAOS-time sweep test (0.005 %, 1 Hz) |
| 15:00–15:30 | CSR test (0.1 $min^{-1}$) | 83:45–84:15 | Resting |
| 15:30–30:00 | Resting | 84:15–106:15 | Strain sweep test (0.001 %–100 %, 1 Hz) |
| 30:00–30:30 | CSR test (0.1 $min^{-1}$) | | |
| 30:30–45:00 | Resting | | |
| 45:00–45:30 | CSR test (0.1 $min^{-1}$) | | |
| 45:30–60:00 | Resting | | |
| 60:00–60:30 | CSR test (0.1 $min^{-1}$) | | |
| 60:30–75:00 | Resting | | |
| 75:00–75:30 | CSR test (0.1 $min^{-1}$) | | |
| 75:30–90:00 | Resting | | |
| 90:00–90:30 | CSR test (0.1 $min^{-1}$) | | |

$$\tau_0 = \frac{\left(\frac{1}{R_1^2} - \frac{1}{R_2^2}\right)}{4\pi h \ln\left(\frac{R_2}{R_1}\right)} G \tag{2}$$

$$\mu = \frac{\left(\frac{1}{R_1^2} - \frac{1}{R_2^2}\right)}{8\pi^2 h} H \tag{3}$$

where $\tau_0$ is the dynamic yield stress (unit: Pa), μ is the plastic viscosity (unit: Pa·s), $R_1$ is the vane radius (unit: mm), $R_2$ is the inner radius of the measuring cell (unit: mm), $h$ is the vane height (unit: mm). Fig. 3(e) indicates that both the dynamic yield stress and the plastic viscosity increase with the CH dosage, and such phenomena are mainly attributed to the small grain size and high SSA of CH. As shown in Table 1, the SSA of CH is 10 times larger than that of limestone. According to Ref [19,34], particles with higher SSA could capture more free water, and therefore lead to lower water film thicknesses [35] (see Eq. (4)). As shown in Fig. 3(e), the increase in dynamic yield stress and plastic viscosity appears to be linked to the reduction of water film thickness, which enhances the particle interaction during the steady flow.

$$WFT = \frac{\phi_{excess}}{SSA_0} \tag{4}$$

$$\phi_{excess} = \phi_{total} - \phi_{void} \tag{5}$$

$$\phi_{void} = \frac{1 - \varphi_m}{\varphi_m} \tag{6}$$

$\phi_{excess}$, $\phi_{total}$ and $\phi_{void}$ denote the excess water volume fraction, the water ratio of the paste and void ratio. $\varphi_m$ is the maximal packing density of solid, which is assumed as 0.64, according to [36,37].

### 3.1.2. Structural build-up

The development of static yield stress with the resting time is reported in Fig. 4(a). The static yield stress increases with the CH content. It should be noted that, for mixture C10, static yield stress at 75 and 90 min were not measured since the torque had gone above the upper limit of the current rheometer (230 mN·m). For the other two mixtures, mixture C0 showed a much lower static yield stress than C2.5 at 15 min. However, the static yield stress development afterwards was significantly different in these two mixtures. As shown in Fig. 4(b), between 15 min and 45 min, the static yield stress increment in C0 is almost twice that in C2.5. As a result, higher static yield stress was observed in C10 at 45 min. After 45 min, the static yield stress developed at a similar rate in both C0 and C2.5.

Fig. 5(a) illustrates the strain sweep test results before and after 60 min of resting time. It can be found that the storage modulus G' increased significantly after 60 min for all the mixtures. Shear stress responses in strain sweep tests are presented in Fig. 5(b). In all the curves obtained after the resting time, peaks were found when the applied strain reached approximately 1 %. In contrast, there was no clear peak in curves measured before 60 min of resting time. According to earlier studies [19,38,39], this peak value could be attributed to the colloidal attractive interaction in cementitious material systems. Fig. 5(c) summarized peak values of shear stresses measured after 60 min of resting time. For mixtures containing CH, both G′ and shear stress increased with the CH content. Before the resting time, mixture C0 showed a similar G′ and shear stress with mixture C2.5. However, after that, G′ and shear stress of mixture C0 were largely boosted and became much higher than those of C2.5.

During the 60 min of resting time, G′ evolution of studied mixtures was monitored using SAOS-time sweep. As shown in Fig. 6(a), G′ of all mixtures developed slowly in the first 10–20 min. In this stage, the

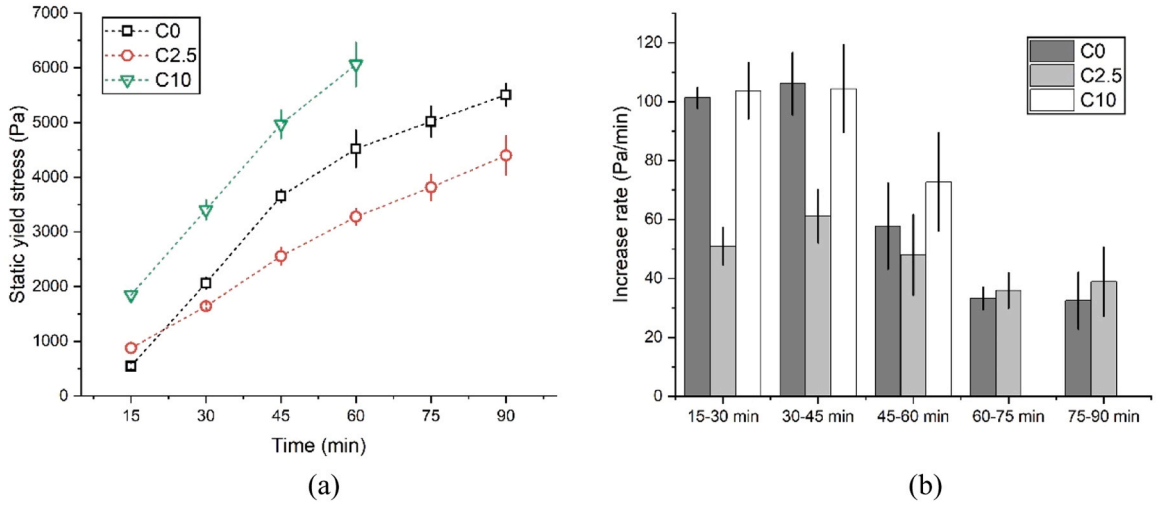


**Fig. 4.** (a) Evolution of static yield stress with time measured by CSR test; (b) The rate of increase in static yield stress between two consecutive test cycles.

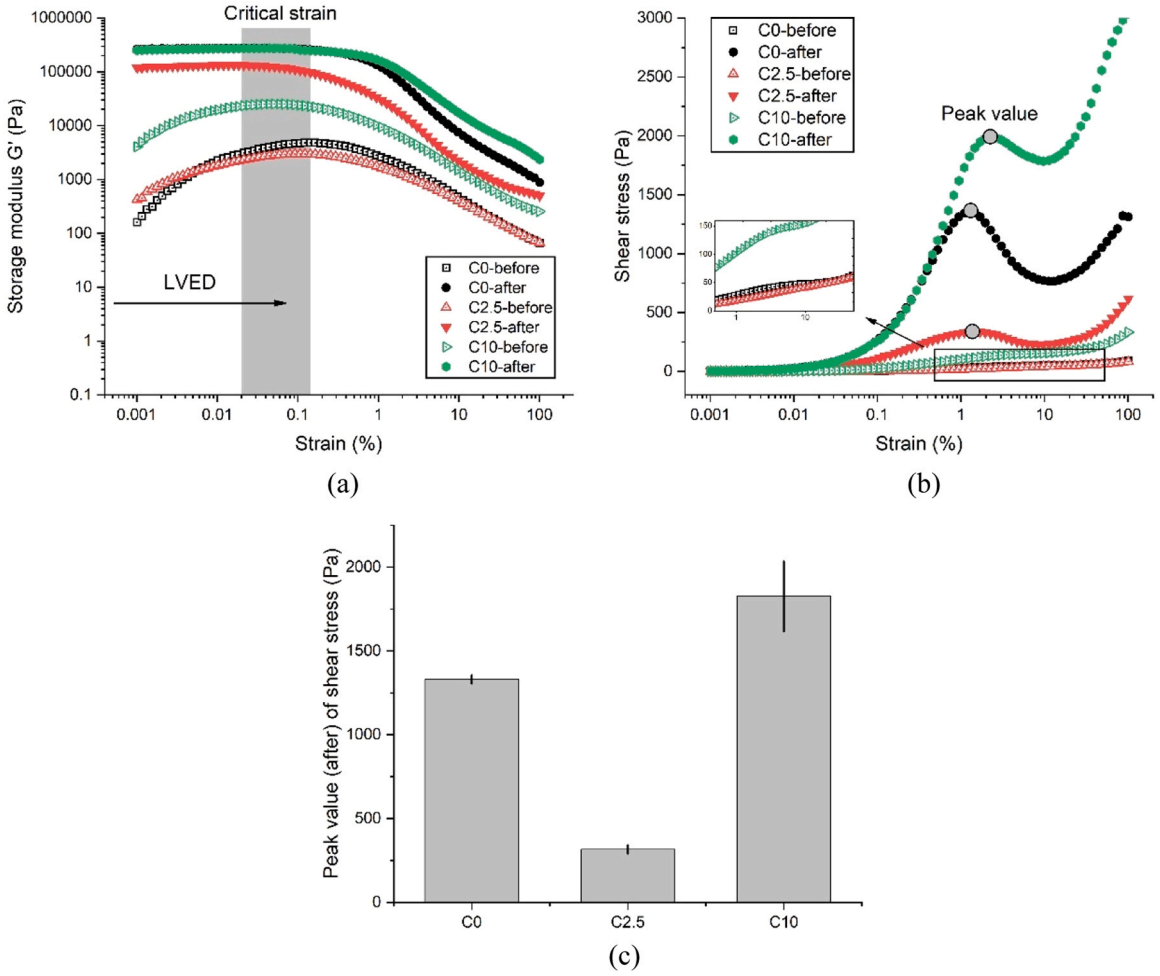


**Fig. 5.** Strain sweep test results: (a) Storage modulus G′ vs. applied strain (0.001 %-100 %); (b) Shear stress vs. applied strain (0.001 %-100 %); (c) Peak values of shear stresses in Fig. 5(b). Before or after indicating the test conducted before or after 60 min' resting (performed when the material age was 23 or 83 min, respectively).

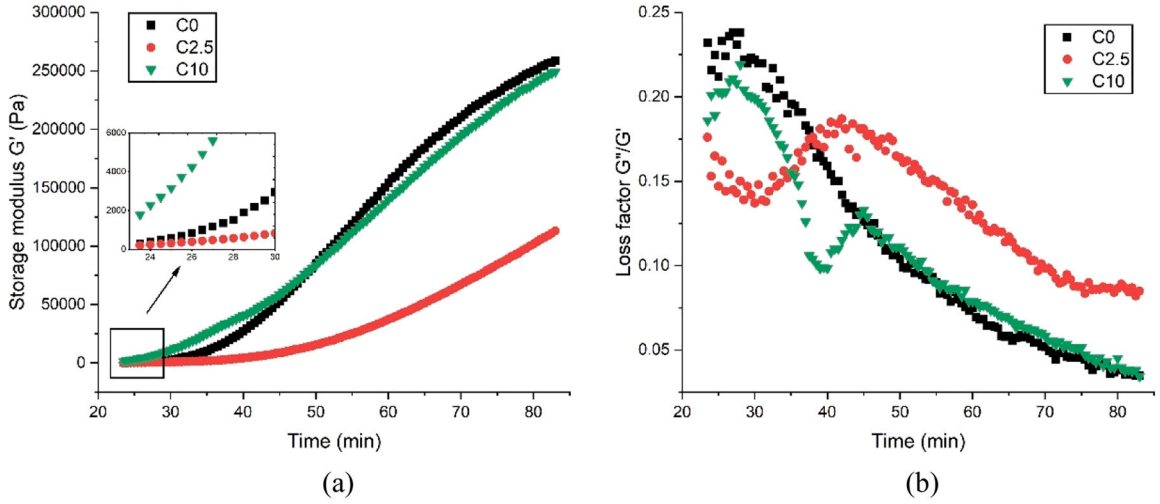


**Fig. 6.** SAOS-time sweep test results (material age: 23–83 min): (a) Evolution of storage modulus G′ with time; (b) Evolution of loss factor G''/G′ with time.

dispersion effect of SP strongly delayed the flocculation of studied mixtures. Mixture C10 showed a much higher G′ and growth rate compared to others. The G′ of C2.5 was slightly lower than that of C0. Afterwards, the development of G′ was enhanced by cement particle flocculation [19,39]. In this stage, G′ increased almost linearly with time, and the slope (i.e., increasing rate) was also influenced by the lime content. Compared to mixture C10, mixture C0 showed a faster G′ development and a shorter transition time (from the first stage to the

second), so after 50 min, the highest G′ was observed in C0. However, differences between C0 and C10 are marginal, and G′ of both mixtures are significantly higher than that of C2.5. Fig. 6(b) presents the loss factor of these mixtures, and at least one peak can be found in the loss factor curve. As mentioned by [40,41], G″ may develop faster than G′ when gelation occurs, so the ratio between them (i.e., the reduction factor) should increase. In this study, gelation seems to be correlated to the effect of SP. After casted, binding material particles were gradually covered by PCE molecules and therefore got more hydrophobic. As a result, captured water molecules were released to increase the proportion of liquid phases. For C0, the loss factor decreased with time after the peak, while for C2.5 and C10, the loss factor decreased first and then increased, so a peak at around 45 min was observed. This phenomenon may be attributed to the reduction of solid phases due to the dissolution of CH and/or the delayed dispersion effect of SP. After this peak, the loss factor of mixture C10 became similar with that of mixture C0. For mixtures C2.5 and C10, increasing the dosage of CH largely decreased loss factor, resulting a high rigidity of fresh mixture.

Overall, adding CH in LC3 system seems to inhibit the evolution of elasticity (see Fig. 6(a)). This is because that the CH particles can be partly dissolved, resulting in the decrease in solid volume fraction, and the increase in calcium concentration, as well as pH of pore solution. The reduction in solid volume fraction caused the increased inter-particle distance, leading to a decrease in colloidal interactions between particles [36]. Besides, as reported by Garrault and Nonat [42], the high initial concentration of calcium hydroxide may reduce the number of CSH nuclei. As mentioned by Roussel et al. [39], the static yield stress is an overlapping result of colloidal interaction, C-S-H nucleation and rigid grain-grain contact. The decrease in colloidal interactions and C-S-H nucleation led to a delayed development of static yield stress over time, particularly in the mixture with a minor addition of CH (mixture C2.5). However, when the CH content reaches 10 %, the adverse effect of CH dissolution on the development of storage modulus and static yield stress with the first 1.5 h is mitigated. The reduction in C-S-H nucleation and solid volume fraction did not significantly affect the evolution of static yield stress and elasticity. However, the underlying mechanism remains complex and unresolved, warranting further investigation into the effect of CH dissolution in future studies.

### 3.2. Hydration kinetics and phase assemblages

#### 3.2.1. Hydration kinetics

Fig. 7(a) demonstrates the normalized heat flow of studied mixtures over the first 7 days. Both the silicate reaction peak and the sulfate depletion peak were clearly observed in all mixtures. For the first peak, the intensity increased with the additional CH content, while for the second one, the influence in intensity is quite limited. Given that rapid early-age reactions are preferred in engineering practice, optimization of the gypsum and hydrated lime should be considered in future studies to ensure that both peaks appear within the first 24 h. Occurrences of

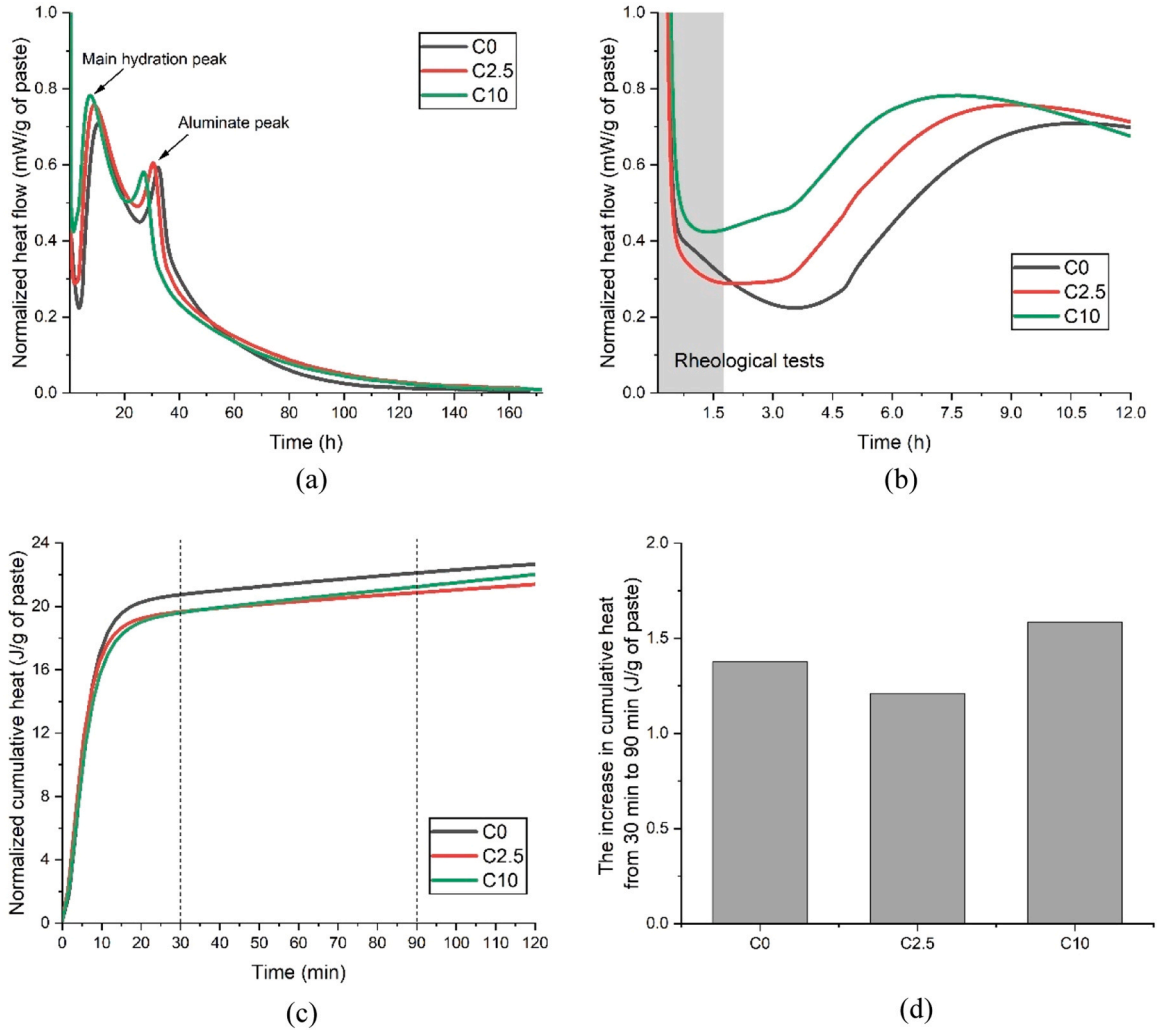


**Fig. 7.** Isothermal calorimetry test results: (a) Heat flow normalized by the mass of paste over time (the first 7 days); (b) Heat flow normalized by the mass of paste over time (the first 12 h); (c) Normalized cumulative heat over the first 2 h; (d) The increase in normalized cumulative heat from 30 to 90 min of studied mixtures.

both peaks were earlier in mixtures with additional CH, suggesting that lime could accelerate the formation of C-S-H and AFm phases. As discussed in earlier studies [43,44], the additional lime provides additional precipitation surface for hydration products, potentially promoting filler effects. However, the rapid dissolution of hydrated lime may result in relatively higher $Ca^{2+}$ concentration in pore solutions, hindering the dissolution of clinker phases and thus slightly delaying hydration reactions in early ages. Therefore, the lowest cumulative heat release was observed in C2.5 between 30 and 90 min (Fig. 7(b) and (d)). It should be noted that, the chemical effect can be compensated by the physical filler effect when the lime content reached a high value. As the result, C10 shows the highest heat flow and cumulative heat values during the period of 30–90 min. This finding also agrees well with the results of static yield stress development (Fig. 4) and the stress peak value of strain sweep test after 60 min of resting (Fig. 5(b) and (c)).

### 3.2.2. Phase assemblages

Fig. 8 shows TG-DTG curves of studied materials at ages of 1 h, 7 days and 28 days, and four clear peaks can be defined in all the figures. In early-age samples (shown in Fig. 8(a)), the peak at around 100°C (peak 1) is related to the dehydration of ettringite and C-S-H, while the peak at around 130°C (peak 2) indicates the water loss from gypsum. However, the latter peak cannot be found in samples at the ages of 7 and 28 days (shown in Fig. 8(b) and (c)). Instead, another peak at around 170°C (peak 5) appeared, and it can be related to the decomposition of AFm phases.

The other two peaks, appeared at around 450°C (peak 3) and 800°C (peak 4), are corresponding to dehydration of $Ca(OH)_2$ and decarbonation of $CaCO_3$, respectively. Contents of these two phases can be further calculated following the tangential method, and results were summarized in Table 5. It should be noted that, other carbonate-contained phases, like carboaluminates, also contributed to the decarbonation peak at around 800°C. Hence, $CaCO_3$ content reported in Table 5 should be slightly higher than the real value. Both phases were consumed during the hydration process, and depletion of $Ca(OH)_2$ was observed in C0 and C2.5 after 7 days. Given that $Ca(OH)_2$ was consumed through both pozzolanic reactions and further reactions with ettringite, more C-(A)-S-H and AFm phases could be formed in C2.5 and C10, so peak 1 and 5 are more significant in these two mixtures. Furthermore, despite the potential negative effect of additional $Ca(OH)_2$ on $CaCO_3$ dissolution and lower initial $CaCO_3$ contents, greater losses in $CaCO_3$ content were observed in C2.5 and C10, suggesting that the additional lime also accelerated the formation of carboaluminates.

This tendency can also be proved with XRD patterns (Fig. 9), as peaks for both hemicarboaluminate (Hc) and monocarboalumiante (Mc) are more pronounced in mixtures with additional lime. It should be noted that, instead of forming Mc, a large amount of Hc was observed after 28

**Table 5**
$Ca(OH)_2$ and $CaCO_3$ contents calculated with TG results (Unit:%).

| Mixture | $Ca(OH)_2$ contents | | | $CaCO_3$ contents | | |
|---|---|---|---|---|---|---|
| | 1 h | 7 d | 28 d | 1 h | 7 d | 28 d |
| C0 | 0.61 | n.a. | n.a. | 24.56 | 22.61 | 21.87 |
| C2.5 | 1.40 | n.a. | n.a. | 22.14 | 19.43 | 18.77 |
| C10 | 6.20 | 2.17 | 1.46 | 15.37 | 14.19 | 13.03 |

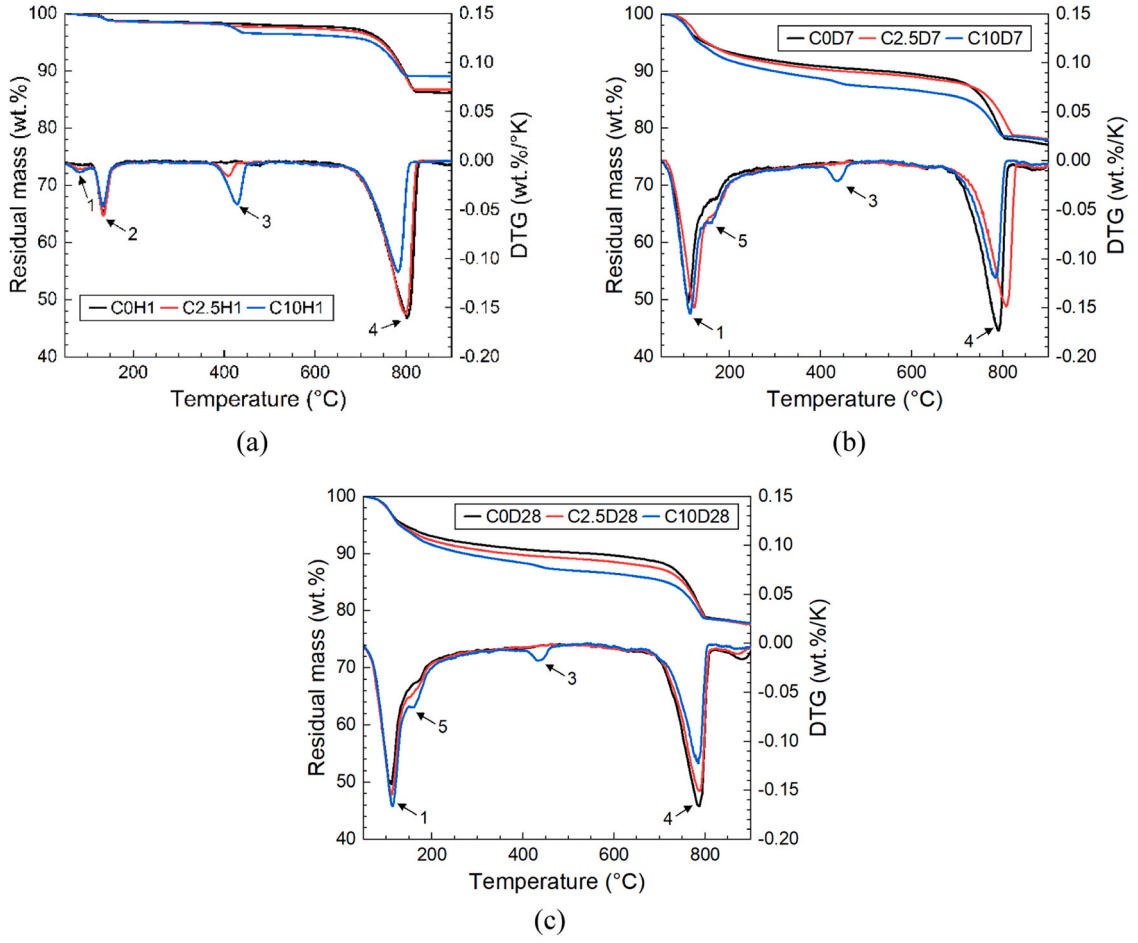


**Fig. 8.** TGA-DTG of mixtures C0, C2.5 and C10 at (a) 1 h, (b) 7 days and (c) 28 days. 1-ettringite and C-S-H; 2-gypsum; 3-calcium hydroxide (CH); 4-calcium carbonate; 5-AFm.

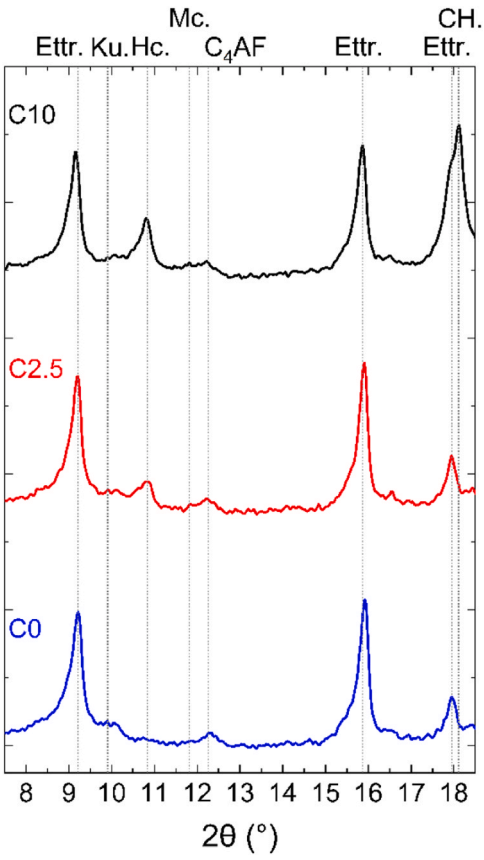


**Fig. 9.** XRD patterns for different mixtures at 28 days. Ettr.-Ettringite, Ku.-Kuzelite, Hc.-Hemicarboaluminate, Mc.-Monocarboaluminate, CH.-Portlandite.

days. A similar phenomenon has been observed in LC3 systems without the addition of CH [45]. This is because the formation of carboaluminates is largely controlled by the availability of $CO_3^{2-}$. At 28 days, due to the limited dissolution rate of $CaCO_3$, Hc is formed, and it may subsequently transform into Mc [46].

More details could be obtained through Rietveld refinements of XRD data (summarized in Table 6). As discussed above, more carboaluninates could be found in lime-rich mixtures. In contrast to the OPC-limestone system, where the formation of carboaluminate hydrates consumes $C_3A$ and thus protects ettringite [47], the investigated system has abundant alumina supplies from calcined clay. With the additional hydrated lime to provide calcium and hydroxyl ions, continuous conversion from ettringite to AFm was detected in C2.5 and C10 [48], as the remained ettringite contents in these two groups were lower. Furthermore, more amorphous contents were detected in mixtures with CH. Despite the fact that there are initial amorphous phases in raw materials (mainly in calcined clay, discussed in Section 2), their influences could be limited, as a consistent calcined clay content was considered in all mixtures. The difference should be mainly attributed to the continuous pozzolanic reactions maintained by the additional CH.

**Table 6**
Rietveld refinement results of XRD patterns (wt%).

| Phases | C0 | C2.5 | C10 |
|---|---|---|---|
| Belite ($C_2S$) | 1.26 | 1.22 | 1.24 |
| Ferrite ($C_4AF$) | 0.45 | 0.55 | 0.68 |
| Quartz | 16.13 | 13.60 | 12.19 |
| Portlandite (CH) | 0.39 | 0.28 | 1.98 |
| Calcite (L) | 19.94 | 16.26 | 12.17 |
| Ettringite | 7.56 | 5.49 | 5.34 |
| Kuzelite | 0.61 | 0.71 | 0.30 |
| Monocarboaluminate (Mc.) | 0.00 | 0.18 | 0.31 |
| Hemicarboaluminate (Hc.) | 0.07 | 0.54 | 2.23 |
| Amorphous | 53.59 | 61.17 | 63.56 |

### 3.3. Microstructures and mechanical properties

#### 3.3.1. Pore structure

Fig. 10 compares the MIP test results of different mixtures at 7 and 28 days. As can be observed, a higher dosage of CH leads to a lower total porosity. In C0 and C2.5, no significant change was observed in either the capillary porosity (pores in the range of 0.01 μm-10 μm) and the effective porosity (the difference between the peak and the final mercury intrusion values) between 7 and 28 days. This phenomenon is in agreement with the phase assemblage analyses in the Section 3.2.2. Due to the depletion of $Ca(OH)_2$ in these mixtures, there is no new products (e.g., C-(A)-S-H gel and AFm) to further refill capillary pores. In C10, due to continuous pozzolanic reactions, the capillary porosity decreased from 20.06 % to 17.74 %, and effective porosity decreased from 8.92 % to 7.13 %. The similar pore refinement effect of the additional CH have been reported elsewhere [22].

However, it should be noted that, more macropores (i.e., pores larger than 10 μm) were observed in C2.5 and C10, and this may be related to the workability loss induced by CH. As discussed in Section 3.1, the viscosity of the fresh paste can be significantly increased by the additional lime, so there is a higher possibility to introduce more air voids into the fresh mixture. As shown in Figs. 11 and 12, The volume of large air voids (diameter>1 mm) is significantly increased by the addition of CH.

#### 3.3.2. Compressive strength

Fig. 13 compares the compressive strength of different studied mixtures at material ages of 1, 3, 7, 28 and 56 days. Despite the fact that more air voids were introduced in C2.5 and C10, their compressive strengths are still higher than those of C0. The addition of hydrated lime enhances both early-age hydration and the pozzolanic reaction, leading to an increased formation of C-(A)-S-H gel and AFm (hemi-carboaluminate), as well as reduced capillary porosity after 7 and 28 days (see Fig. 10). This is the main reason for the higher compressive strengths observed in C2.5 and C10 compared to C0. However, this does not necessarily mean that the influence of fresh properties does not exist. After 28 days, the compressive strength of C10 is slightly lower than that of C2.5, but this difference can be further compensated by continuous pozzolanic reactions in the former mixture. Therefore, after 56 days, the compressive strength of C10 is higher than those of other mixtures.

## 4. Conclusions

In this study, impacts of additional hydrated lime on fresh and hardened properties of limestone–calcined clay cementitious materials with a high level of Portland cement replacement (80 wt% of the binder), especially its effects on rheological properties and related microstructure changes, was experimentally investigated. Main findings of this work were concluded as follows:

- Due to the high specific surface area (SSA) of hydrated lime (more than 10 times that of limestone), replacing a portion of limestone with hydrated lime significantly reduced the water film thickness. This reduction resulted in enhanced dynamic yield stress, plastic viscosity, and re-flocculation, particularly at rotational velocities lower than 10 $min^{-1}$.
- The minor addition of hydrated lime led to a delay in the development of storage modulus within the first 1.5 h. However, this effect was mitigated by increasing the dosage of hydrated lime (mixture C10). The acceleration of structural build-up (evolution of static yield stress) induced by 10 wt% of hydrated lime can be attributed to the increased colloidal interaction and/or rigid grain-grain contact.

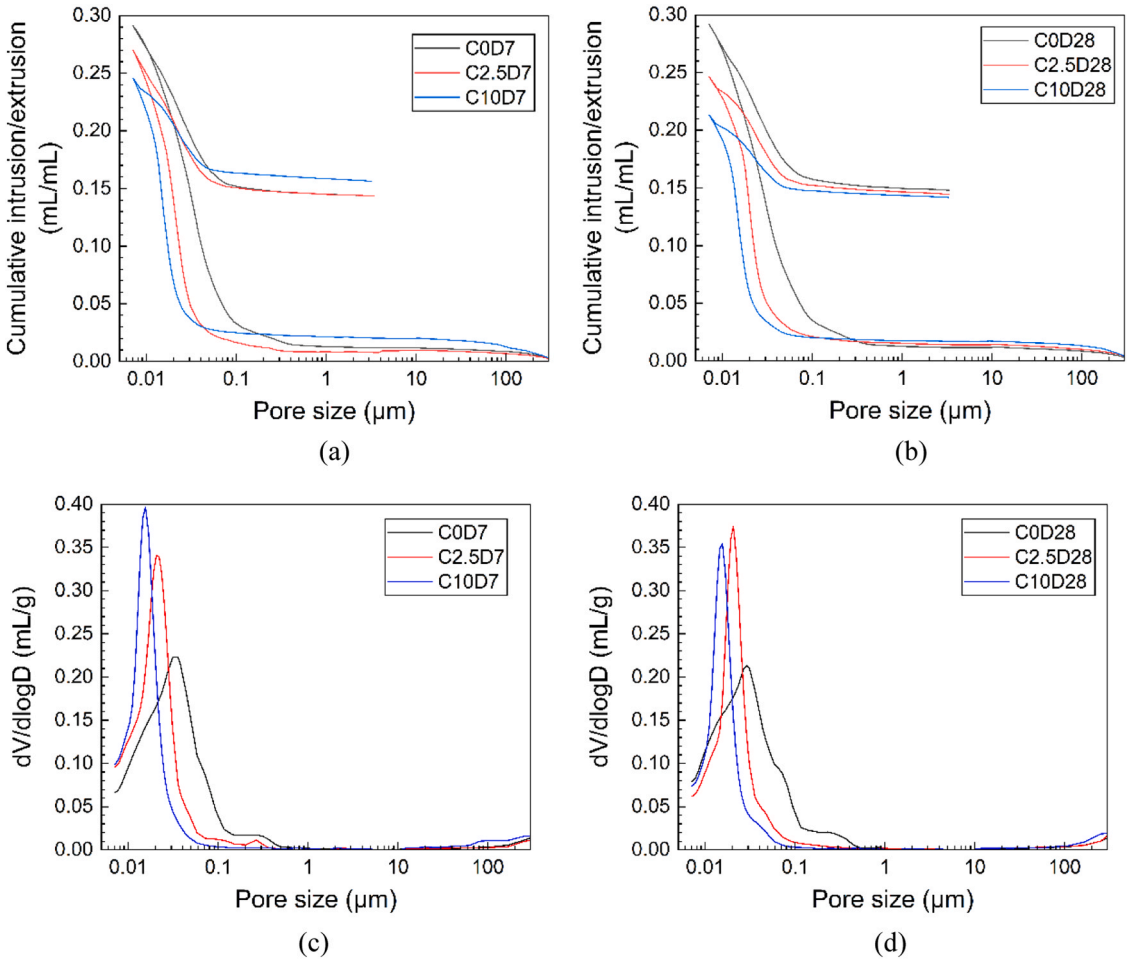


**Fig. 10.** MIP results of different mixtures at 7 days (D7) and 28 days (D28). (a) and (b) Cumulative intrusion/extrusion curve; (c) and (d) Pore size distribution.

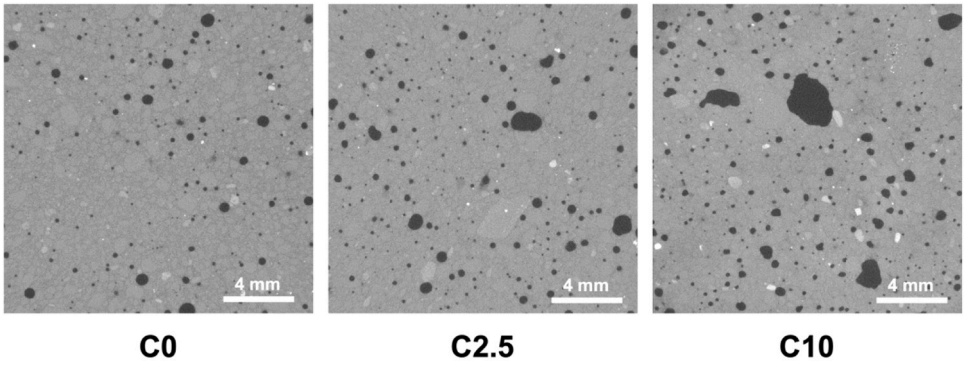


**Fig. 11.** Grayscale images of different mixtures obtained by X-CT scanning.

- The addition of hydrated lime accelerated early-age hydration, resulting in a higher intensity of the main hydration peak compared to the reference mixture. Additionally, the presence of hydrated lime contributed to the sustained occurrence of the pozzolanic reaction, leading to an increased amount of C-(A)-S-H gel and AFm (hemicarboaluminate), and reduced capillary porosity after 7 and 28 days. These findings are consistent with the results reported by Sun et al. [12].
- Despite the reduction in flowability and the introduction of high air void contents, mixtures with hydrated lime still exhibited significantly higher compressive strength at 56 days compared to the reference mixture (C0). The mixture with 10 wt% of hydrated lime and only 20 wt% Portland cement (C10) can eventually achieve a compressive strength of more than 40 MPa.

This study indicates that adding a relatively small dosage (up to 10 wt%) of hydrated lime into the low-clinker LC3 system could help to enhance long-term pozzolanic reactions, densify the microstructure and improve the compressive strength. However, due to its extremely high SSA, hydrated lime could have negative impacts on the flowability and therefore lead to a higher air void content. Therefore, special care should be taken when designing the amount of additional hydrated lime. Furthermore, given that the additional hydrated lime may increase the $CO_2$ emissions of LC3, further optimization of the hydrated lime content

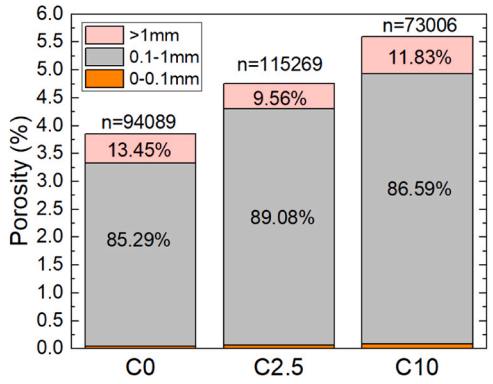


**Fig. 12.** Air void size distributions (pore size> 12.5 μm) of studied mixtures. *n* refers to the number of air voids in each sample.

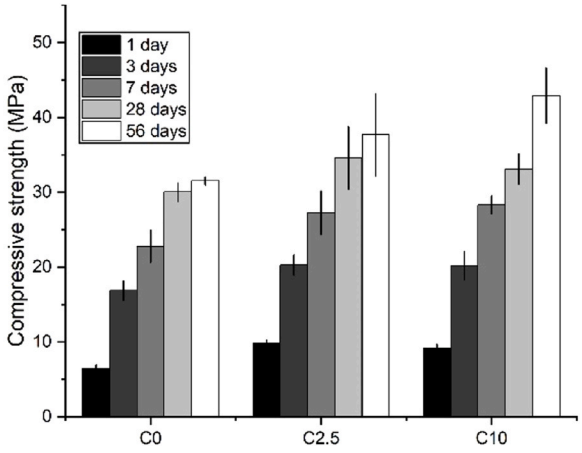


**Fig. 13.** Compressive strength of studied mixtures at 1, 3, 7, 28 and 56 days.

is necessary to balance long-term performance and life-cycle carbon footprint.

## CRediT authorship contribution statement

**Oğuzhan Çopuroğlu:** Writing – review & editing. **Minfei Liang:** Writing – review & editing, Investigation. **Shan He:** Writing – review & editing, Investigation. **Yu Chen:** Writing – review & editing, Writing – original draft, Visualization, Validation, Methodology, Investigation, Formal analysis, Data curation, Conceptualization. **Yu Zeng:** Writing – review & editing, Writing – original draft, Visualization, Validation, Methodology, Investigation, Formal analysis, Data curation.

## Declaration of Competing Interest

On behalf of all the authors, I declare that all authors have no conflict of interest regarding the content of the research as written in the submitted article.

## Acknowledgments

Yu Chen would like to acknowledge the funding supported by National Natural Science Foundation of China (NSFC) (Grant No. 52402021), Natural Science Foundation of Jiangsu Province (Grant No. BK20241338), the Start-up Research Fund of Southeast University (Grant No. RF1028624009).

## Appendix

**Table A1**
Mixtures designed for the preliminary isothermal calorimetry screening (Unit: wt% of the binder)

| | Portland cement | Calcined clay | Limestone powder | Additional gypsum | Water | SP |
|---|---|---|---|---|---|---|
| 0 % additional gypsum | 20 | 50 | 30 | 0 | 30 | 1 |
| 2 % additional gypsum | 20 | 50 | 28 | 2 | 30 | 1 |
| 4 % additional gypsum | 20 | 50 | 26 | 4 | 30 | 1 |
| 6 % additional gypsum | 20 | 50 | 24 | 6 | 30 | 1 |

## Data availability

Data will be made available on request.

## References

[1] R. Snellings, P. Suraneni, J. Skibsted, Future and emerging supplementary cementitious materials, Cem. Concr. Res. 171 (2023), https://doi.org/10.1016/j.cemconres.2023.107199.
[2] M.C.G. Juenger, F. Winnefeld, J.L. Provis, J.H. Ideker, Advances in alternative cementitious binders, Cem. Concr. Res. 41 (2011) 1232–1243, https://doi.org/10.1016/j.cemconres.2010.11.012.
[3] Y. Zhang, M. He, L. Wang, J. Yan, B. Ma, X. Zhu, Y.S. Ok, V. Mechtcherine, D.C. W. Tsang, Biochar as construction materials for achieving carbon neutrality, Biochar 4 (2022), https://doi.org/10.1007/s42773-022-00182-x.
[4] K. Scrivener, F. Martirena, S. Bishnoi, S. Maity, Calcined clay limestone cements (LC3), Cem. Concr. Res. 114 (2018) 49–56, https://doi.org/10.1016/j.cemconres.2017.08.017.
[5] F. Avet, R. Snellings, A. Alujas Diaz, M. Ben Haha, K. Scrivener, Development of a new rapid, relevant and reliable (R3) test method to evaluate the pozzolanic reactivity of calcined kaolinitic clays, Cem. Concr. Res. 85 (2016) 1–11, https://doi.org/10.1016/j.cemconres.2016.02.015.
[6] M. Antoni, J. Rossen, F. Martirena, K. Scrivener, Cement substitution by a combination of metakaolin and limestone, Cem. Concr. Res. 42 (2012) 1579–1589, https://doi.org/10.1016/j.cemconres.2012.09.006.

[7] M. Sharma, S. Bishnoi, F. Martirena, K. Scrivener, Limestone calcined clay cement and concrete: a state-of-the-art review, Cem. Concr. Res. 149 (2021) 106564, https://doi.org/10.1016/j.cemconres.2021.106564.
[8] J. Skibsted, R. Snellings, Reactivity of supplementary cementitious materials (SCMs) in cement blends, Cem. Concr. Res. 124 (2019) 105799, https://doi.org/10.1016/j.cemconres.2019.105799.
[9] F. Zunino, K. Scrivener, Microstructural developments of limestone calcined clay cement (LC3) pastes after long-term (3 years) hydration, Cem. Concr. Res. 153 (2022) 106693, https://doi.org/10.1016/j.cemconres.2021.106693.
[10] Y. Dhandapani, T. Sakthivel, M. Santhanam, R. Gettu, R.G. Pillai, Mechanical properties and durability performance of concretes with limestone calcined clay cement (LC 3), Cem. Concr. Res. 107 (2018) 136–151, https://doi.org/10.1016/j.cemconres.2018.02.005.
[11] F. Zunino, K. Scrivener, The reaction between metakaolin and limestone and its effect in porosity refinement and mechanical properties, Cem. Concr. Res. 140 (2021) 106307, https://doi.org/10.1016/j.cemconres.2020.106307.
[12] J. Sun, F. Zunino, K. Scrivener, Hydration and phase assemblage of limestone calcined clay cements (LC3) with clinker content below 50%, Cem. Concr. Res. 177 (2024) 107417 https://doi.org/10.1016/j.cemconres.2023.107417.
[13] S. Bishnoi, S. Maity, A. Mallik, S. Joseph, S. Krishnan, Pilot scale manufacture of limestone calcined clay cement: the Indian experience, Indian Concr. J. 88 (2014) 22–28.
[14] A.C. Emmanuel, P. Haldar, S. Maity, S. Bishnoi, Second pilot production of limestone calcined clay cement in India: the experience, Indian Concr. J. 90 (2016) 57–63.
[15] L.M. Vizcaíno-Andrés, S. Sánchez-Berriel, S. Damas-Carrera, A. Pérez-Hernández, K.L. Scrivener, J.F. Martirena-Hernández, Industrial trial to produce a low clinker, low carbon cement, Mater. Constr. 65 (2015) e045, https://doi.org/10.3989/mc.2015.00614.
[16] A. Parashar, F. Avet, M. Canut, K.A. Riding, B. Wang, T. Sui, S. Vieira, E.F. Irassar, L. Velasquez, R.S. Almenares-Reyes, K.C. Thienel, M. Maier, F. Kanavaris, F. Zunino, G. Escadeillas, M.Ben Haha, M.C.G. Juenger, T. Hanein, S. Bishnoi, F. Martirena-Hernández, Industrialisation of calcined clay cements: past, present, and future: a paper of RILEM TC 282-CCL, Mater. Struct. Constr. 57 (2024) 1–23, https://doi.org/10.1617/s11527-024-02488-7.
[17] EN 197-1, Cement - Part 1: Composition, specifications and conformity criteria for common cements, NEN. (2000) 178–184. https://doi.org/10.1016/0005-2736(80)90400-9.
[18] Y. Chen, S. He, Y. Zhang, Z. Wan, O. Çopuroğlu, E. Schlangen, 3D printing of calcined clay-limestone-based cementitious materials, Cem. Concr. Res. 149 (2021) 106553, https://doi.org/10.1016/j.cemconres.2021.106553.
[19] Y. Chen, Y. Zhang, B. Šavija, O. Çopuroğlu, Fresh properties of limestone-calcined clay-slag cement pastes, Cem. Concr. Compos 138 (2023) 104962, https://doi.org/10.1016/j.cemconcomp.2023.104962.
[20] G. Zhang, G. Peng, X. Zuo, X. Niu, H. Ding, Adding hydrated lime for improving microstructure and mechanical properties of mortar for ultra-high performance concrete, Cem. Concr. Res. 167 (2023) 107130, https://doi.org/10.1016/j.cemconres.2023.107130.
[21] R. Jaafri, A. Aboulayt, S.Y. Alam, E. Roziere, A. Loukili, Natural hydraulic lime for blended cement mortars: behavior from fresh to hardened states, Cem. Concr. Res. 120 (2019) 52–65, https://doi.org/10.1016/j.cemconres.2019.03.003.
[22] C. Hu, Y. Tao, B.P. Gautam, F. Wang, Performance enhancement of sustainable cementitious material with ultrahigh content limestone and calcined clay, ACS Sustain. Chem. Eng. 10 (2022) 10733–10742, https://doi.org/10.1021/acssuschemeng.2c03688.
[23] A. Laveglia, L. Sambataro, N. Ukrainczyk, N. De Belie, E. Koenders, Hydrated lime life-cycle assessment: current and future scenarios in four EU countries, J. Clean. Prod. 369 (2022) 133224, https://doi.org/10.1016/j.jclepro.2022.133224.
[24] M. Chabannes, H. Kazemi-kamyab, J. Trigallez, R. Snellings, Performance and microstructure development of lime – calcined fluvial sediment binders under different curing conditions, Cem. Concr. Res. 160 (2022) 106903, https://doi.org/10.1016/j.cemconres.2022.106903.
[25] NEN-EN 196-2, Method of testing cement - Part 2: Chemical analysis of cement, (2013).
[26] M. Haist, J. Link, D. Nicia, S. Leinitz, C. Baumert, T. von Bronk, D. Cotardo, M. Eslami Pirharati, S. Fataei, H. Garrecht, C. Gehlen, I. Hauschildt, I. Ivanova, S. Jesinghausen, C. Klein, H.W. Krauss, L. Lohaus, D. Lowke, O. Mazanec, S. Pawelczyk, U. Pott, N.W. Radebe, J.J. Riedmiller, H.J. Schmid, W. Schmidt, E. Secrieru, D. Stephan, M. Thiedeitz, M. Wilhelm, V. Mechtcherine, Interlaboratory study on rheological properties of cement pastes and reference substances: comparability of measurements performed with different rheometers and measurement geometries, Mater. Struct. Constr. 53 (2020), https://doi.org/10.1617/s11527-020-01477-w.
[27] X. Dai, S. Aydın, M.Y. Yardımcı, K. Lesage, G. De Schutter, Effects of activator properties and GGBFS/FA ratio on the structural build-up and rheology of AAC, Cem. Concr. Res. 138 (2020) 106253, https://doi.org/10.1016/j.cemconres.2020.106253.
[28] D. Jiao, K. El Cheikh, C. Shi, K. Lesage, G. De Schutter, Structural build-up of cementitious paste with nano-Fe3O4 under time-varying magnetic fields, Cem. Concr. Res. (2019), https://doi.org/10.1016/j.cemconres.2019.105857.
[29] R. Snellings, J. Chwast, Ö. Cizer, N. De Belie, Y. Dhandapani, P. Durdzinski, J. Elsen, J. Haufe, D. Hooton, C. Patapy, M. Santhanam, K. Scrivener, D. Snoeck, L. Steger, S. Tongbo, A. Vollpracht, F. Winnefeld, B. Lothenbach, RILEM TC-238 SCM recommendation on hydration stoppage by solvent exchange for the study of hydrate assemblages, Mater. Struct. 51 (2018) 172, https://doi.org/10.1617/s11527-018-1298-5.
[30] Y. Chen, O. Çopuroğlu, C.R. Rodriguez, F.F. de Mendonca Filho, E. Schlangen, Characterization of air-void systems in 3D printed cementitious materials using optical image scanning and X-ray computed tomography, Mater. Charact. 173 (2021) 110948, https://doi.org/10.1016/j.matchar.2021.110948.
[31] NEN-EN 196-1, Methods of testing cement - Part 1: Determination of strength, (2016).
[32] N. Roussel, Steady and transient flow behaviour of fresh cement pastes, Cem. Concr. Res. 35 (2005) 1656–1664, https://doi.org/10.1016/j.cemconres.2004.08.001.
[33] M. Thiedeitz, T. Kränkel, C. Gehlen, Viscoelastoplastic classification of cementitious suspensions: transient and non-linear flow analysis in rotational and oscillatory shear flows, Rheol. Acta 61 (2022) 549–570, https://doi.org/10.1007/s00397-022-01358-9.
[34] Y. Chen, Y. Zhang, S. He, M. Liang, Y. Zhang, E. Schlangen, Rheology control of limestone calcined clay cement pastes by modifying the content of fine- grained metakaolin, J. Sustain. Cem. Mater. 0 (2023) 1–15, https://doi.org/10.1080/21650373.2023.2169965.
[35] W.W.S. Fung, A.K.H. Kwan, Role of water film thickness in rheology of CSF mortar, Cem. Concr. Compos 32 (2010) 255–264, https://doi.org/10.1016/j.cemconcomp.2010.01.005.
[36] N. Roussel, A. Lemaître, R.J. Flatt, P. Coussot, Steady state flow of cement suspensions: a micromechanical state of the art, Cem. Concr. Res. 40 (2010) 77–84, https://doi.org/10.1016/j.cemconres.2009.08.026.
[37] Y. Chen, C.R. Rodriguez, Z. Li, B. Chen, O. Çopuroğlu, E. Schlangen, Effect of different grade levels of calcined clays on fresh and hardened properties of ternary-blended cementitious materials for 3D printing, Cem. Concr. Compos 114 (2020) 103708, https://doi.org/10.1016/j.cemconcomp.2020.103708.
[38] A. Favier, J. Hot, G. Habert, N. Roussel, J.B. D'Espinose De lacaillerie, flow properties of MK-based geopolymer pastes. A comparative study with standard portland cement pastes, Soft Matter 10 (2014) 1134–1141, https://doi.org/10.1039/c3sm51889b.
[39] N. Roussel, G. Ovarlez, S. Garrault, C. Brumaud, The origins of thixotropy of fresh cement pastes, Cem. Concr. Res. 42 (2012) 148–157, https://doi.org/10.1016/j.cemconres.2011.09.004.
[40] P. Steins, A. Poulesquen, O. Diat, F. Frizon, Structural evolution during geopolymerization from an early age to consolidated material, Langmuir 28 (2012) 8502–8510, https://doi.org/10.1021/la300868v.
[41] Y. Chen, Y. Zhang, S. He, X. Liang, E. Schlangen, O. Çopuroğlu, Improving structural build-up of limestone-calcined clay-cement pastes by using inorganic additives, Constr. Build. Mater. 392 (2023) 131959, https://doi.org/10.1016/j.conbuildmat.2023.131959.
[42] S. Garrault, A. Nonat, Hydrated layer formation on tricalcium and dicalcium silicate surfaces: experimental study and numerical simulations, Langmuir 17 (2001) 8131–8138, https://doi.org/10.1021/la011201z.
[43] O. Cizer, Competition between Carbonation and Hydration on the Hardening of Calcium Hydroxide and Calcium Silicate Binders, KU Leuven, 2009.
[44] M. Fourmentin, P. Faure, S. Gauffinet, U. Peter, D. Lesueur, D. Daviller, G. Ovarlez, P. Coussot, Porous structure and mechanical strength of cement-lime pastes during setting, Cem. Concr. Res. 77 (2015) 1–8, https://doi.org/10.1016/j.cemconres.2015.06.009.
[45] H. Du, S.D. Pang, High-performance concrete incorporating calcined kaolin clay and limestone as cement substitute, Constr. Build. Mater. 264 (2020) 120152, https://doi.org/10.1016/j.conbuildmat.2020.120152.
[46] A. Ipavec, R. Gabrovšek, T. Vuk, V. Kaučič, J. MačEk, A. Meden, Carboaluminate phases formation during the hydration of calcite-containing portland cement, J. Am. Ceram. Soc. 94 (2011) 1238–1242, https://doi.org/10.1111/j.1551-2916.2010.04201.x.
[47] D. Wang, C. Shi, N. Farzadnia, Z. Shi, H. Jia, Z. Ou, A review on use of limestone powder in cement-based materials: mechanism, hydration and microstructures, Constr. Build. Mater. 181 (2018) 659–672, https://doi.org/10.1016/j.conbuildmat.2018.06.075.
[48] T. Matschei, B. Lothenbach, F.P. Glasser, The AFm phase in portland cement, Cem. Concr. Res. 37 (2007) 118–130, https://doi.org/10.1016/j.cemconres.2006.10.010.